

# Laser beam welding of an Oxide Dispersion Strengthened super alloy

H. J. K. Lemmen · K. J. Sudmeijer · I. M. Richardson ·  
S. van der Zwaag

Received: 30 January 2006 / Accepted: 3 April 2006 / Published online: 31 January 2007  
© Springer Science+Business Media, LLC 2007

**Abstract** Laser beam welding was used successfully to join the Oxide Dispersion Strengthened Super alloy PM1000 for a range of welding conditions. A microscopical study revealed a disturbed structure of dendrites and micro sized particles, which were formed during the molten state of the weld process. Although the particles are a result of melting and clustering of the yttrium oxide particles, tensile tests at high temperatures showed only a minor decrease of strength. It is found that the morphology of the weld, which is closely related to the heat input, has a strong influence on its failure behavior at elevated temperatures.

## Introduction

PM1000 (MA754) is an Oxide Dispersion Strengthened Super alloy (ODS-alloy) developed for high temperature applications with an excellent corrosion and oxidation resistance and the capability of carrying loads up to 90% of the melting temperature [1]. These properties are valuable for the application of PM1000 in Thermal Protection Systems (TPS) of reentry space

vehicles [2, 3]. To produce a TPS, joining technologies are needed [4] that meet the requirements for reentry. ODS-alloys contain small, thermodynamically stable, ceramic particles, which provide the high temperature mechanical properties [5]. The dispersion strengthening is strongly dependent on the size (typically on the order of 30 nm diameter) and the spatial distribution of the particles [6, 7]. The only available method to incorporate these particles into the alloy is by sintering of nano-sized powders. ODS-alloys are considered to be non fusion-weldable because of the clustering behavior of the ceramic particles during the liquid state [8]. However, laser beam welding [9–12] can possibly provide a solution as it has a very local heat input and therefore a minimal Heat Affected Zone (HAZ). During welding a keyhole is formed by the equilibrium between the surface tension of the liquid metal and the plasma pressure inside the keyhole. To form the keyhole the temperature must rise above the boiling points of nickel and chromium which are respectively 2732 °C and 2672 °C. Because of the extremely high temperature gradient inside the weld [13], a strong fluid flow in the melt exists. The fluid flow is expected to have a large influence on the dispersion of the yttrium oxide particles. The flow in combination with the thermal gradients and applied heating and cooling rates, results in a microstructure that is significantly modified compared with its optimized state created during sheet production [14].

The aim of the research was to determine the process window for laser beam welding of ODS alloys and to relate the welding parameters to the microstructure and the high temperature mechanical properties. In this research we demonstrate that laser beam welding of PM1000 is not only possible but also that

---

H. J. K. Lemmen (✉) · K. J. Sudmeijer ·  
S. van der Zwaag  
Faculty of Aerospace Engineering, Delft University of  
Technology, Kluyverweg 1, Delft 2629 HS, The Netherlands  
e-mail: H.J.K.Lemmen@lr.tudelft.nl

I. M. Richardson  
Faculty of Material Science & engineering, Delft University  
of Technology, Rotterdamseweg 137, Delft 2628 AL,  
The Netherlands

the high temperature strength properties of the weld are exceptionally good.

## Experimental

### Material composition

For this research PM1000 (Ni–20Cr–0.30Al–0.50Ti–0.60Y<sub>2</sub>O<sub>3</sub>–1.00Fe–0.05C wt.%) [15] sheet material, produced by Plansee GmbH, with a thickness of 1 mm was used. The alloy has a large grain structure, as a result of a heat treatment (1350 °C) and the rolling process, to improve the creep properties at high temperatures. The grains have a thickness of 10–40 µm and a width and length in the order of 10–15 mm. Tensile tests were performed along the principle rolling direction (L) while welding was performed perpendicular to the principle rolling direction (LT).

### Laser beam welding process

A 3 kW HAAS HL3006D Nd:YAG laser was used for the welding experiments. The laser light is transported to the laser head through a 600 µm glass fiber. The focusing optic has a focal length of 150 mm and projects a laser spot of 450 µm diameter on the work piece. The focal plane was determined experimentally by marking spots on the surface of a black anodized aluminum plate with short pulses (power 700 W and time 30 ms) and varying the defocusing of the beam. The focal point was fixed on the upper surface of the samples ( $Z = 0$ ).

A shielding gas of industrial pure argon was delivered to the work piece by two trailing copper tubes each with a diameter of 15 mm positioned at the upper side, in line with each other. Gas from the first tube protects the molten weld pool whilst gas from the rear tube protects the hot metal after solidification. The lower surface was protected by argon gas in an enclosed groove below the weld track. During the welding process the amount of shielding gas at the upper surface was 32 L/min and at the lower surface 7 L/min.

13 Bead-on-plate welds and 2 butt welds (weld 8 and 15) were welded with varying weld parameters to determine the optimum process window (Table 1). To evaluate the morphology of the welds, the cross sectional area of each individual weld was measured which has, in combination with the heat input (P/v), a strong relation to the Energy Transfer Efficiency (ETE) and the Melting Efficiency. Samples characteristic for the various morphologies are discussed below.

**Table 1** Welding parameters

Weld number	Power [W]	Speed [mm/s]	P/v [J/mm]
1	2750	120	22.92
2	3000	120	25.00
3	1500	60	25.00
4	2750	100	27.50
5	2250	80	28.13
6	1750	60	29.17
7	3000	100	30.00
8	3000	100	30.00
9	2500	80	31.25
10	2000	60	33.33
11	2750	80	34.38
12	1500	40	37.50
13	2250	60	37.50
14	1750	40	43.75
15	3000	60	50.00

### Microscopy

For the microscopical observations the samples of the welds were embedded and polished to a 1 µm diamond finish. The specimens were etched for 10 s with a solution of the following composition: 1 part glacial acetic acid (C<sub>2</sub>H<sub>4</sub>O<sub>2</sub>), 1 part 65% nitric acid (HNO<sub>3</sub>), and 1 part 30% hydrochloric acid (HCL).

Optical microscopy was performed with a Leica microscope with an objective of 60 × to 110 ×.

For the identification of elements and high magnification observations, a SEM (JEOL; JSM-840A) with a ThermoNoran EDX system was used. The resolution of this SEM is 12 nm at a working distance (W) of 39 mm under perfect circumstances. For most samples an acceleration voltage of 15 kV and a working distance of 39 mm was used. The penetration depth of the EDX was on the order of 100 nm.

### Mechanical properties

To evaluate the mechanical properties, tensile tests on three welds (weld 3, 8 and 15) were performed at elevated temperatures. For the high temperature tensile tests a Gleeble 3500 was used. The dog-bone specimens were made according to standard EN 10002-5. The specimens were clamped mechanically between copper blocks. Slippage was prevented by two steel pins with a diameter of 5 mm, which fitted through a hole in the clamping area of the test specimen. The temperature was measured using a thermocouple attached to the middle of the specimen, which provided a feedback to control the current through the specimen. The clamps were cooled, but the temperature in the test area of the specimen was found to be homogeneous within 20 °C.

The specimens were heated with a rate ( $\dot{T}$ ) of 30 °C/s. The temperature was stabilized for 20 s before the tensile tests were started. The tests were position controlled with a displacement rate of 0.036 mm/s. After fracture the samples were cooled in air. All tensile tests were conducted in a low vacuum.

The results of the tensile tests on the welded material were compared with the results from the tensile tests on the parent material. Six temperatures were chosen in the range from 20 °C up to 1250 °C. The parent material and weld 3 were tested at all six temperatures, whilst weld 8 and 15 were only tested at 1200 °C and 1250 °C. The fracture surfaces from the tensile tests were analyzed with the SEM and optical microscopy.

A further evaluation of the welds was done by Vickers microhardness tests at 0.5 N. The tests were performed along a transverse line through the middle of the weld. Prior to the hardness measurement the specimens were polished and etched for 2 s to determine the location of the fusion boundary.

## Results

All welds were successfully produced with no spatter during welding and no visual post-weld cracking. The welds were symmetrical and did not show any gravity effects. The amount of oxidation was higher at the lower side of the samples than at the upper side. All welds were fully penetrated except for weld 1 which was partly penetrated with a closed keyhole.

## Microscopy results

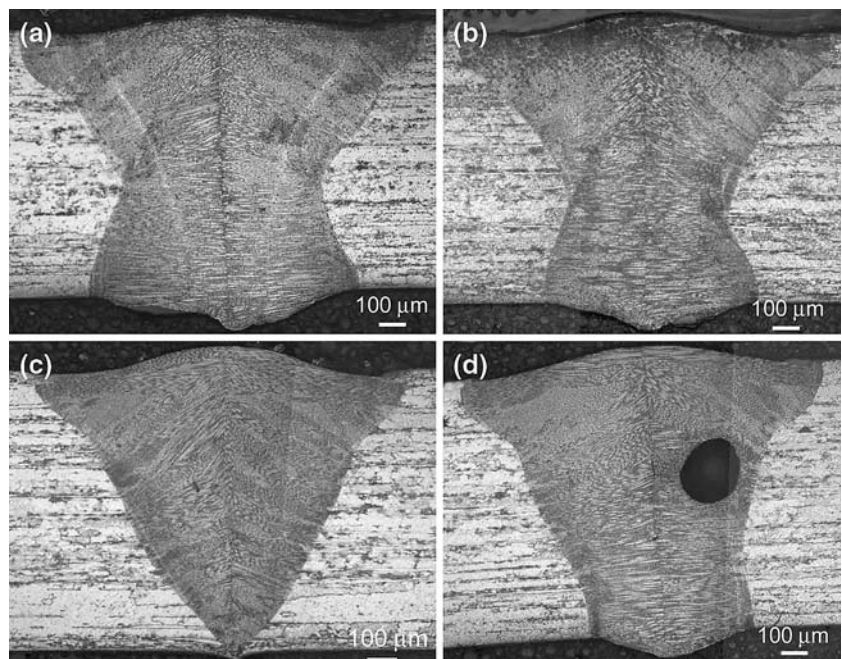
The cross sections of all welds, except weld 1, showed a similar geometry, only the size of the welds showed variations (Fig. 1a, –d). The size of each weld was measured and the cross sectional area was related to the heat input as shown in Fig. 2. The butt welds are smaller than the bead-on-plate welds made with the same weld parameters. A typical result that occurred in every weld is bulging of the weld surface indicating that the material was pressed out. The increase of the height ( $\Delta t$ ) is in the order of 15% to 20% with respect to the original sheet thickness.

The fusion zone is clearly recognizable by the dendritic structures [14]. A sharp border is found between the grain structures of the parent material and the dendritic structure of the fusion zone (Fig. 3a). There is no visible heat affected zone at either side of the weld.

The orientation of dendritic growth is parallel to the thermal gradient, as in almost all cases of laser beam welding [16]; therefore the orientation of the dendritic grain structure is perpendicular to the borders of the weld. In every weld a centerline is visible where the grains from both sides met during the solidification process (Fig. 3b). At welding speeds above 80 mm/s instabilities, such as an asymmetric centerline or a gas porosity, were found in some welds (Fig. 3c). At lower welding speeds no such defects were encountered.

Figures 3a and b show round particles (encircled) with a size of a few microns. These particles are also detected by the SEM. The particles differ in size from

**Fig. 1** Microscopic photographs of: a; weld 12 ( $v = 40$  mm/s,  $P = 1500$  W), b; weld 6 ( $v = 60$  mm/s,  $P = 1750$  W), c; weld 1 ( $v = 120$  mm/s,  $P = 2750$  W), d; weld 2 ( $v = 120$  mm/s,  $P = 2750$  W)





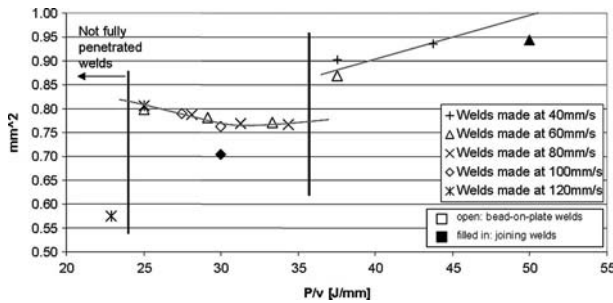


**Fig. 2** Cross sectional area of the welds [mm<sup>2</sup>] as a function of the heat input [J/mm]

0.1 to 10 μm and are equally dispersed over the fusion zone. Similar particles densities are found in the various welds. EDX analyses showed that the particles contain primarily yttrium, aluminum and titanium (with an average from the EDX results of 23% Al,

8% Ti, and 69% Y). At the top and bottom of most welds a slag-like material structure is visible (Fig. 3d). With EDX analyses it is found that this material contain the same elements, with the same ratios as the particles in the weld area.

**Tensile test results**

The engineering stress–strain curves from all tests on the parent material and the welded material show low scatter and good reproducibility. Three stress–strain curves of the parent material for different temperatures are shown in Fig. 4a. The engineering stress–strain curves for the welded material and those for the parent material are plotted for three temperatures (Fig. 4b– d). The results from the mechanically tests on the welded material are compared by normalizing these results to the mechanical properties found for the parent material (Fig. 5b–d).

**Fig. 3** Optical micrographs of: (a) border of the weld (arrows) and micron sized particles (circles), (b) center line of the weld (arrows) and micron sized particles (circles), (c); weld structure due to instabilities in weld 2 made at a high welding speed (100–120 mm/s), (d) Islands of slag like material at surface of the weld

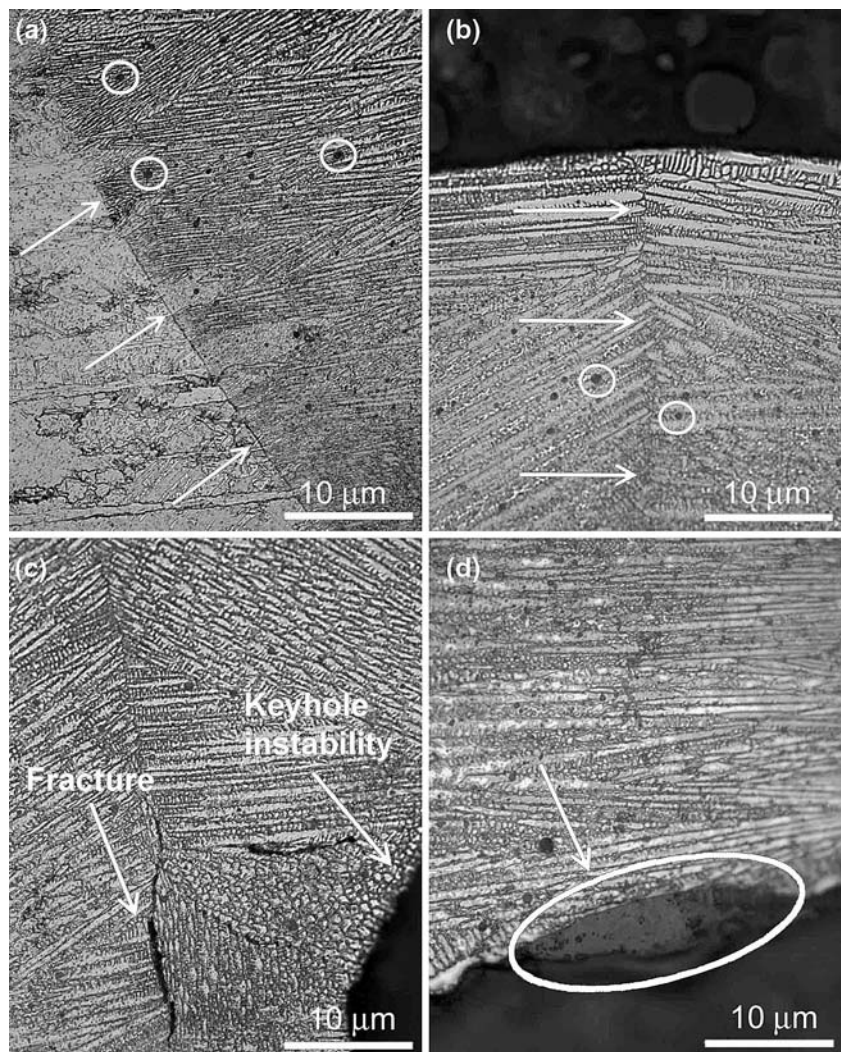
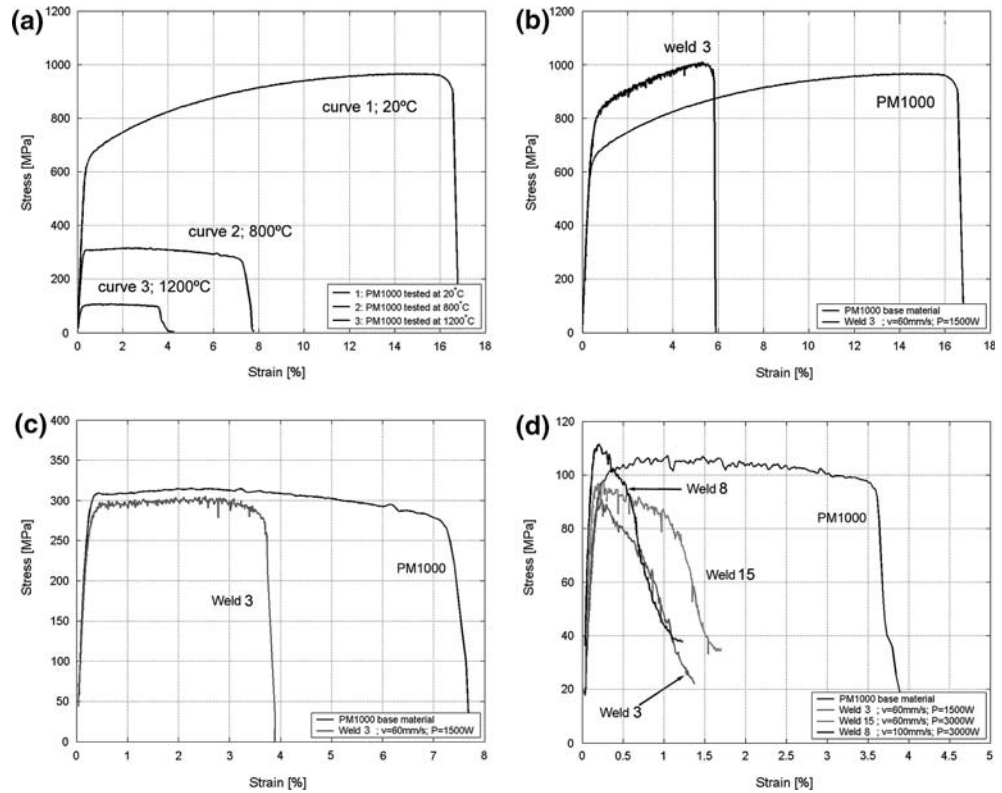


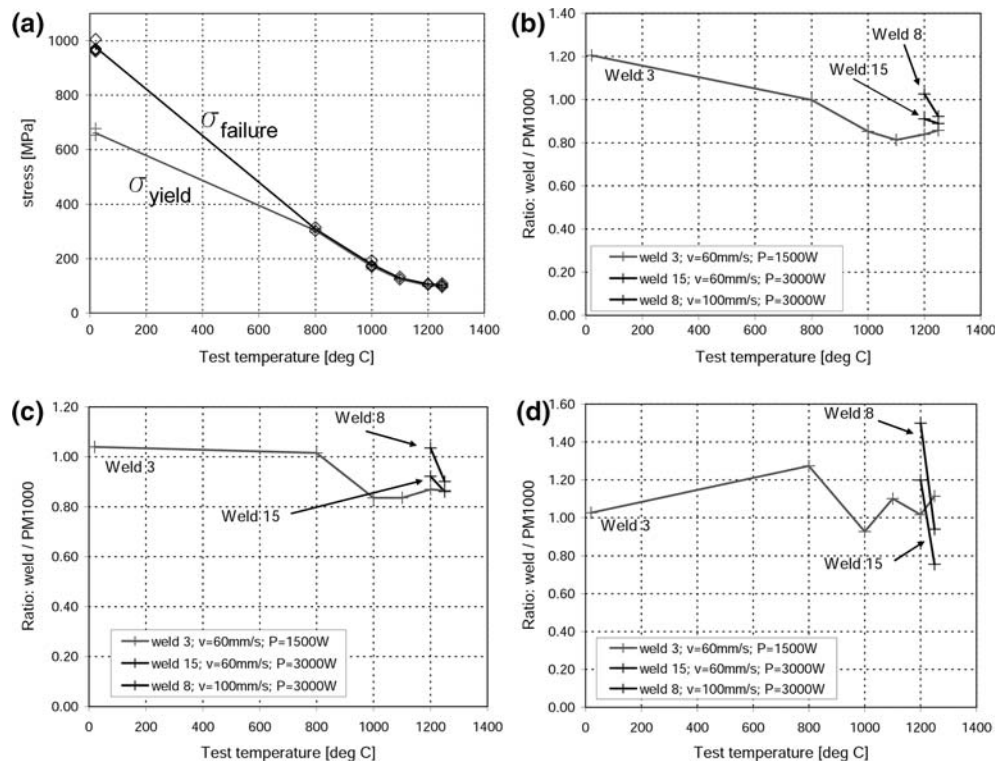
**Fig. 4** Stress strain curves of: (a) parent material tested at 20, 800 and 1200 °C. (b) parent material and weld 3 tested at 20 °C, (c) parent material and weld 3 tested at 800 °C, (d) parent material and weld 3, weld 8 and weld 15 tested at 1200°C



The tests on the parent material shows several temperature related changes including a decrease of the Young’s modulus, the yield stress, the failure stress,

and the failure strain (Fig. 5a). The plastic regions of the stress–strain curves experience a temperature related change, from a plastic region with strain

**Fig. 5** (a) temperature relation of the yield stress and failure stress for the parent material, (b); normalized yield stress of weld 3, 8 and 15 as a function of temperature, (c); normalized failure stress of weld 3, 8 and 15 as a function of temperature, (d); normalized stiffness of weld 3, 8 and 15 as a function of temperature



hardening, to a perfect elastic-plastic region at elevated temperatures. Due to the absence of strain hardening, early necking strongly reduces the failure strain during uniaxial testing.

The tests on the welded material show the same temperature related trends as for the parent material. Only the plastic region shows at higher temperatures a different trend. At 20 °C and 800 °C the failure strain of the weld is approximately 35% of that of the parent material. At temperatures above 800 °C the failure strain of the welded material decreases to 20% of that of the parent material. At temperatures above 800 °C the welded samples show strain softening.

**Hardness test results**

Three hardness profiles of typical welds are given in Fig. 6. The hardness profiles show a decrease of 70 HV in the fusion zone and an increase of 40 HV around the fusion zone, compared to the hardness of the parent material (290 HV). The hardness profiles show a sharp drop at the boundaries of the fusion zones.

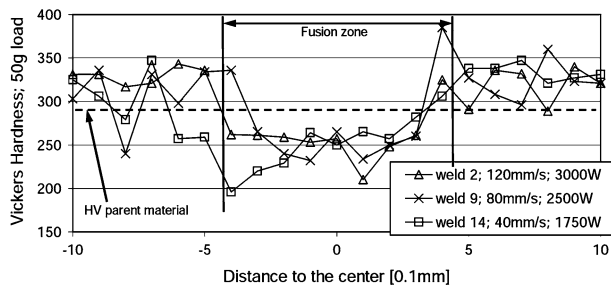


**Fig. 6** Hardness profile from weld 2, weld 9 and weld 14

**Fracture surface analysis**

The side view of the fracture surfaces show a temperature related change of the failure mode in both the parent material and the welded material (Fig. 7). All welded specimens failed in the weld (Fig. 7b, d, f). At 20 °C the specimens failed with an angle of 45° (Figure 7a, b). At elevated temperatures the parent material shows a crumbling structure which indicates an intergranular failure, this is also the case for the weld. The fracture in the weld at elevated temperatures tends to follow the dendritic structure with a preference for the borders of the weld. At temperatures of 1200 °C and higher the failure mechanism is changed and the specimens fail at the centerline of the weld. The fracture is extremely straight and the fracture surface is flat and exactly in the middle of the weld.

Figure 8 shows the fracture surfaces of the parent material and characteristic welds. Figure 9 presents the regions marked in Fig. 8 at a higher magnification. At room temperature the fracture of the parent material and the weld is trans-granular with many dimple rupture. In the dimples of the welds particles are visible with varying sizes from barely visible to a few micron, this is not the case for the parent material. The fractures of the parent material and the weld become both inter-granular above 800 °C. In the upper and lower zone of the weld the fracture is parallel to the dendritic grain structure while in the center region the fracture surface is perpendicular to the principal dendrite axis. At 1200 °C the fractures of the welds show a flat surface perpendicular to the dendritic grain structure. The grain boundaries between the dendrites are visible and at some locations a dendrite is pulled out from the surface.

**Fig. 7** Photographs of the failed tensile test specimen of: (a) parent material tested at 20 °C, (b) weld 3 tested at 20 °C, (c); parent material tested at 800 °C, (d); weld 3 tested at 800 °C, (e); parent material tested at 1200 °C, (f); weld 3 tested at 1200 °C

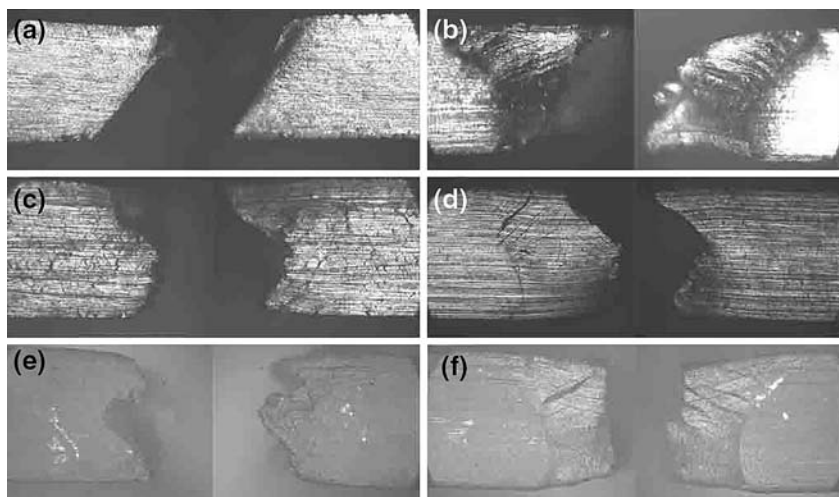
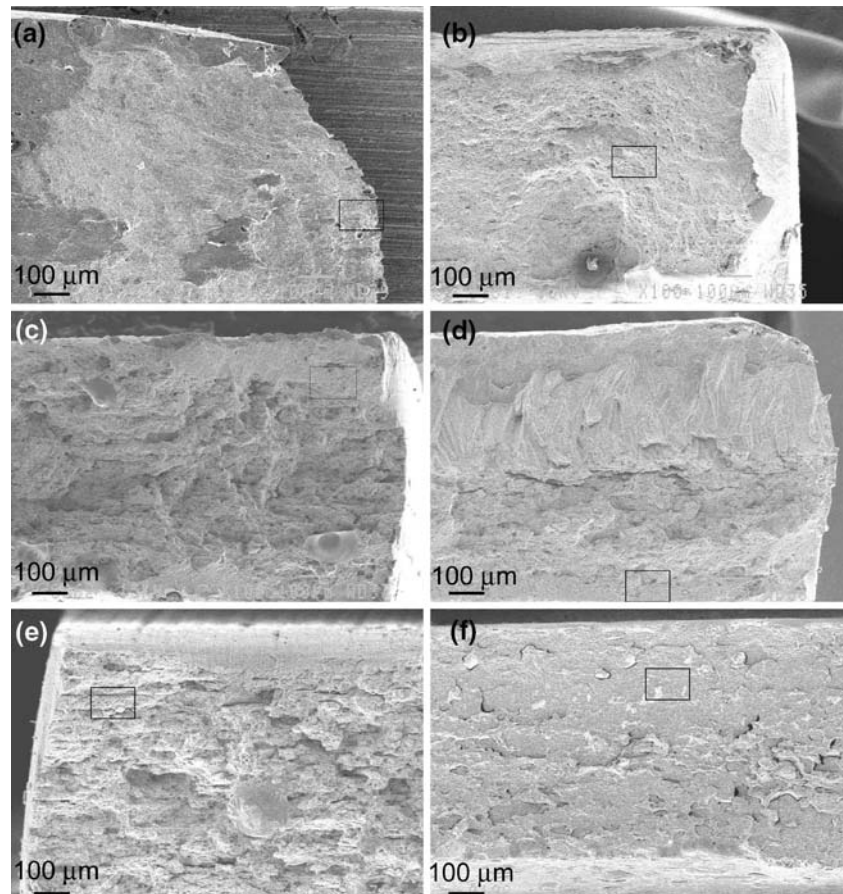




**Fig. 8** SEM photographs of the fracture surfaces of: (a); parent material tested at 20 °C, (b); weld 3 tested at 20 °C, (c); parent material tested at 800 °C, (d); weld 3 tested at 800 °C, (e); parent material tested at 1200 °C, (f); weld 8 tested at 1200 °C



## Discussion

### Morphology of the weld

The optical images show a clear and reproducible geometry of the weld. The borders are sharp and are formed by a temperature boundary in the material, equal to the melt temperature of PM1000: 1410 °C. The shape of the weld is a result of the direction of the heat transport through the sheet in combination with the influence of the penetration of the laser beam and can be explained with the aid of Fig. 10. The laser beam hits the sheet of metal and starts to heat the solid material. The heat is transported in all directions and the metal starts to melt resulting in a V-shaped fusion zone. This geometry was obtained for a heat input < 24 J/mm. The welds of this type are unfavorable because of two reasons: the a-symmetrical morphology of the weld result in a non-uniform load transfer, and the welding process is unstable because a small change of welding parameters results in an incomplete joint.

At higher energy input levels local vaporization causes the pool surface to indent, the beam penetrates the sheet and a keyhole is completed. If more energy is

transported to the material, the weld zone will grow wider because more heat is conducted to the surrounding material. In the middle of the sheet there is more surrounding material to conduct the heat than at the bottom and topside of the weld. Therefore the upper and lower part of the weld are wider.

When the laser beam penetrates the material, energy is lost because the penetrated light will not contribute to the heating of the material. Therefore, after full penetration the weld growth rate decreases significantly for unit increase in beam power. For PM1000 sheet material with a thickness of 1 mm the best welds are produced with a heat input between 24 J/mm and 36 J/mm.

Figure 2 shows that butt welds are smaller than the bead-on-plate welds; this is explained by the loss of energy due to partial dissipation of the laser beam through the small gap between the two sheets which is not present in the bead-on-plate welds.

A characteristic feature of the cross sectional shape of the weld is the bulging of the upper and lower surfaces. Here the molten material is pushed out during welding, by stresses that occur due to the heating up of the material around the weld. The

**Fig. 9** SEM photographs of the fracture surfaces of: (a); parent material tested at 20 °C, (b); weld 3 tested at 20 °C, (c); parent material tested at 800 °C, (d); weld 3 tested at 800 °C, (e); parent material tested at 1200 °C, (f); weld 8 tested at 1200 °C

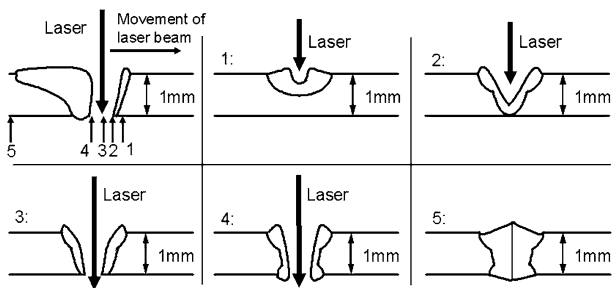
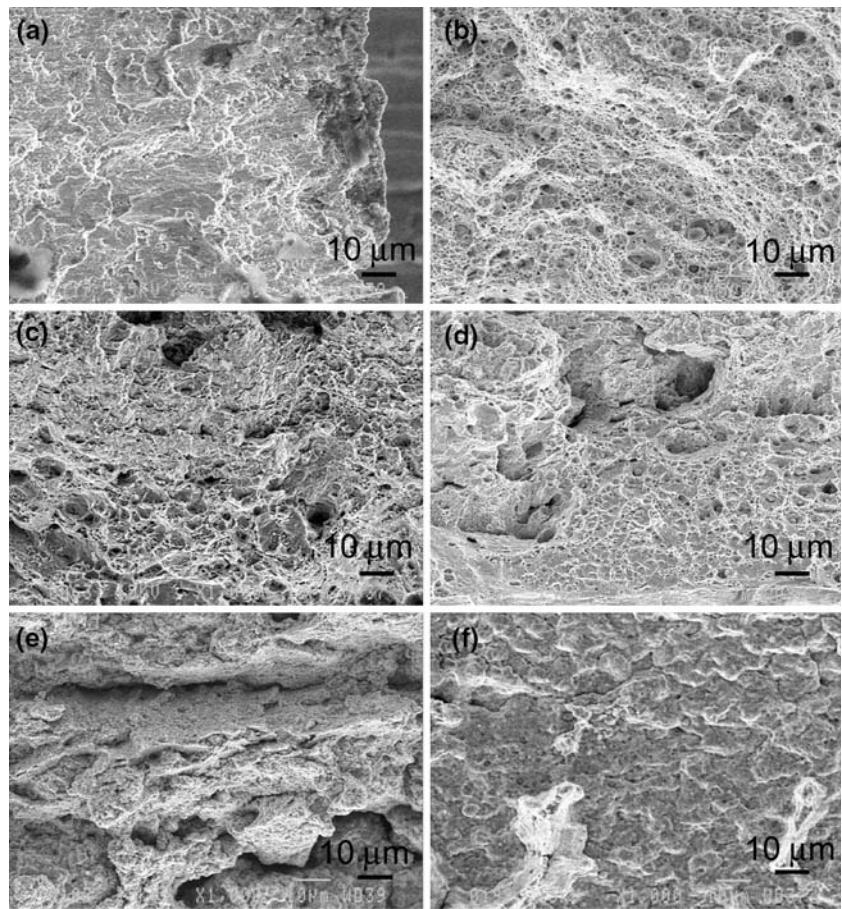


**Fig. 10** Illustration of the laser beam welding process containing one side view and 5 cross sections of the welding process. Each cross section is related to one of the locations in the side view

molten material does not return to its original geometry because the fusion zone solidifies rapidly behind the laser beam, before the compressive stresses have disappear. The non-reversible process results in residual stresses and residual plastic deformations. Those plastic deformations are visible in the stress–strain curves at room temperature as a pre-deformation effect, which will increase the yield stress and reduce the effective failure strain of the material.

### Mechanical properties

As shown in Fig. 4 the failure strains of the welded specimens are much smaller than for the parent material. This is a result of the varying material properties in the welded specimens, resulting in local plasticity only in the weld. The material around the weld does not reach its yield stress or reaches it later. At 20 °C and 800 °C the yield point of the material around the weld is reached, at 1200 °C this is not the case which explains the large difference in plastic deformation between these curves. Weld 15 shows a larger failure strain at 1200 °C than weld 3 and 8, which is a direct effect of the larger width of the weld and therefore a larger ability to deform plastically.

The high failure stress of the weld at 20 °C is explained by the increased true stress in the weld because of the local high plastic deformations resulting in geometrical changes and internal stresses. The increased yield stress however cannot be explained by an increase of true stress due to plastic deformations because the strain at yield is too small to reduce the true stress this much. As described earlier, the material



around the weld experiences some deformations during welding because of the thermal stresses. Figure 4b shows that a pre-deformation of  $\pm 3\%$  should occur at room temperature to obtain this effect. This is 18.75% of the total possible plastic deformation before failure. Because the failure strain decreases by increasing temperature, the strain for such a pre-deformation effect decreases at elevated temperature. For instance at 800 °C and 1200 °C 18.75% of the total plastic strain is a deformation of respectively 1.3% and 0.7%. It is likely that during welding the material heats up to such a high temperature and that during expansion of the weld these deformations occur. The pre-deformation effects give rise to the increase in the Vickers hardness of the material outside the fusion zone. Finally it should be pointed out that the drop in mechanical properties at high temperatures is mainly due to real temperature dependence but is also affected by the annealing of the internal stresses.

#### Fracture surfaces

The change in failure mode shown by the fracture surfaces is supported by the results of the tensile tests. The transition of the failure mode, from an intergranular failure through the whole weld to an intergranular failure over the centerline of the weld above 1100 °C, results in a relative increase of the tensile strength and yield strength of the weld. The fact that the relative reduction of the mechanical properties has a maximum at 1000 °C to 1100 °C and that the changes in the fracture mechanism occur at the same temperature, suggest a strong relation between the fracture mechanism and the mechanical properties. This supports also the small difference between weld 3 and 15 because at high temperatures all welds fail at the centerline. This failure behavior is not influenced by the size of the weld.

#### Origin of the structure in the SEM images

Although the SEM images did not show significantly different structures in the welds, there are still some interesting anomalies found that need explanation. In every weld, irrespective of the location in the weld, a large amount of black spots are visible. The fact that the particles are spread evenly throughout the whole weld zone indicates that no macro segregation of the particles due to buoyancy occurred.

The particles contain yttrium and aluminum and in most cases also titanium and are formed during welding when the material is super heated. Yttrium oxide has a melting temperature of 2430 °C which is

easily reached. If a constant thermal gradient is assumed in the melt between the solid border and the keyhole (with an estimated temperature of the vaporization temperature), then 24% of the molten material is above the melt temperature of yttrium oxide. This is a worst-case scenario because in reality a non-linear thermal gradient is expected in the fusion zone.

When yttrium oxide melts the yttrium segregates with titanium and aluminum because of the low density of these elements compared to nickel and chromium. The largest part of these elements is spread and forms round droplets. A small part of these elements segregates to the surface during welding. This explains the slag like material found in the microscopic images. When the material cools down the three elements are trapped at the same location.

Considering the amount of yttrium, aluminum and titanium, there is enough material to form the particles of this size and distribution, even when only 24% of the yttrium oxide is melted. The fact that most yttrium oxide particles are still in their original state has also been reported in the literature [9].

A proof, of only a small part of the yttrium oxide being lost in the large particles, is found by calculating the other way around. With a tetragonal approach of the volume there is a ratio found between the volume of a particle with a certain diameter and the parent material, needed to form that specific particle. If in 24% of the molten material in the fusion zone the yttrium oxide is used to form new particles there is, in the case of weld 8, a volume of  $3.83 \cdot 10^{-3} \text{ mm}^3$  per mm weld length available to form the deviating particles. This volume is enough to form  $7.49 \cdot 10^{15}$  particles with a diameter of 1  $\mu\text{m}$  with an interparticle distance of 10  $\mu\text{m}$ , which is less than found in the SEM images. 5% of the volume is enough to form the particles with a size of 2  $\mu\text{m}$  to 5  $\mu\text{m}$  and a distribution equal to that found in the SEM images. 7% Of the volume is enough to form the slag material on the weld surfaces. With this calculations it is found that the approximated loss of 24% of the yttrium oxide, is a conservative approach.

When the contribution of the Orowan stress to the yield stress is calculated with the assumption that 24% of the yttrium oxide is lost, than the weakening is about 10% at 1000 °C. This explains partly the larger reduction of the yield stress of the welds found in the tests. The results, found above, can therefore not explain which strength mechanism has the largest effect on the overall mechanical properties. The difference can be a result of other effects like the introduction of the larger (weakening) micron sized

particles or the increase of the amount of grain boundaries. However, looking at the results of weld 8 and weld 15 at 1200 °C it seems that there is room for improvement of the mechanical properties by optimizing the welding process further.

## Conclusions

PM1000 sheet material with a thickness of 1 mm shows very good laser weldability for a large range of welding parameters. The welds are reproducible and predictable. The best welds are obtained at a heat input of 24–36 J/mm and a weld speed of 0.1 m/s.

Considering the relative small losses of failure strength and yield strength, laser beam welding is suitable for applications in thermal protection systems of reentry space vehicles made out of PM1000.

For these welding conditions the (Orowan) strength of the alloy at room and elevated temperatures is almost retained.

The temperature depended fracture mechanics of the welds has a strong relation with the failure strength and yield strength at elevated temperatures.

The small failure strains found in the tensile tests are in reality large deformations applied on a small region of the test specimen. For high temperature applications these strains are of no concern as long as the stress level is below the yield strength of the weld.

## References

1. Wasilkowska A et al (2003) *J Mater Process Technol* 133:218
2. Walpot L, Ottens H (2003) Preparing for atmospheric re-entry with EXPERT's help. *ESA bulletin* 114
3. Blosser ML (2000) Advanced metallic thermal protection systems for reusable launch vehicles. Ph. D. thesis. University of Virginia
4. Krishnardula VG et al (2004) Joining of ferritic oxide dispersion strengthened alloys. International Symposium of Research Students on Material Science and Engineering Chennai India
5. Donachie MJ, Donachie SJ (2002) Super alloys, a technical guide ISBN 0-87170-749-7, ASM international, Materials park
6. Zeizinger H (1986) Werkstoff schädigung in einer ODS-superlegierung Durch hochtemperatur ermüdung und kriechen. ISBN 3-18-142105-7 Max planck Institut
7. Schroder JH (1987) Elektronen mikroskopische untersuchung der hoch temperatur hartungsmechanismus in einer ODS-superlegierung. ISBN 3-18-143105-2 Dusseldorf
8. Gessinger GH (1984) Powder metallurgy of super alloys. ISBN 0-408-11033-3 London butterworths
9. Kelly TJ (1979) Pulsed YAG laser welding of ODS alloys. ISSN: 0094-243X/79/500215-06\$1.50, The International Nickel Company, Inco Research & Development Center Sterling Forest, Suffern, USA
10. Molian PA et al (1992) *J Mater Sci* 27:2687
11. David SA et al (1999) Welding of nickel based superalloy single crystals, ISSN 0043-2288, *Welding in the World* 43(6):6–17
12. Schubert E et al (2001) *J Mater Process Technol* 115:2
13. Haidemenopoulos GN (2001) *J Alloy Comp* 320:302
14. Hu B, Richardson IM (2005) *J Laser Appl* 17:2
15. Material Data Sheet ODS - super alloy; PM1000, Plansee GmbH
16. Bhadeshia HKDH (2000) Directional recrystallisation & its exploitation in mechanically alloyed metals. Proceedings, 21st Riso International Symposium on Materials Science, Roskilde, Denmark, p 15–28